

Inversion of Electrochemical Impedance Spectra based on the Mellin Transform

Anis Allagui**

*Dept. of Sustainable and Renewable Energy Engineering,
University of Sharjah, Sharjah 27272, United Arab Emirates[†] and
Dept. of Electrical and Computer Engineering, Florida International University, Miami, FL33174, United States*

Sohaib Majzoub

Dept. of Electrical Engineering, University of Sharjah, Sharjah 27272, United Arab Emirates

Ahmed Elwakil

*Dept. of Electrical Engineering, University of Sharjah, Sharjah 27272, United Arab Emirates
Nanoelectronics Integrated Systems Center, Nile University, Cairo 12588, Egypt and
Dept. of Electrical and Software Engineering, University of Calgary, Calgary, Alberta T2N 1N4, Canada*

In this work, we show that the Fredholm integral equations underlying the distribution of relaxation times (DRT), the distribution of capacitive times (DCT), and related frameworks share a common mathematical structure, namely that of a Mellin convolution. This comes from the fact that all standard impedance (impedance or admittance) kernels depend on the product $\omega\tau$ rather than on ω and τ independently. Exploiting this structure, we derive an exact algebraic inversion formula in Mellin space that converts the deconvolution problem into a closed-form relation between the Mellin transform of the measured impedance and that of the unknown distribution function. The framework is validated analytically on a set of examples including the constant phase element (CPE), the Davidson-Cole (DC) model, and the finite-length Warburg model with blocking boundary conditions. It is also validated numerically using the fast Mellin transform via the fast Fourier transform algorithm for both the CPE and the DC model, including their DRT and DCT recovery under clean and noisy conditions. The approach unifies the impedance- and admittance-based inversions under a single spectral framework, and provides a new approach for the characterization of electrochemical systems from impedance data.

I. INTRODUCTION

Electrochemical impedance spectroscopy (EIS) is among the most widely used characterization techniques in electrochemistry, by providing frequency-resolved information about charge transfer, diffusion, interfacial adsorption, as well as electrode geometry [1–6]. The challenge in interpreting EIS data is to identify the physical processes that contribute to the measured response, and at what timescales they operate [7]. The standard approach is based on fitting the data with an equivalent circuit model, which requires a topology to be assumed a priori [8–10], and therefore introduces subjectivity and may limit the generality of the conclusions [11, 12]. Alternatively, the distribution of relaxation times (DRT) [7, 13–18] is based on the mapping of the impedance in its frequency domain ($Z(j\omega)$, with ω the angular frequency) to the time domain (i.e. τ -domain of relaxation times) via the Fredholm integral equation of the first kind [16]:

$$Z(j\omega) = \int_0^{\infty} \ker(j\omega, \tau) f(\tau) d\tau \quad (1)$$

where $\ker(j\omega, \tau)$ is a kernel function, and $f(\tau)$ is the desired function.

As an example, a passive impedance admitting a representation in terms of elementary Voigt models (resistor R and capacitor C in parallel, with time constant $\tau = RC$) can be represented in terms of the discrete sum [19]:

$$Z(j\omega) = R_{\infty} + \frac{g_1}{1 + j\omega\tau_1} + \frac{g_2}{1 + j\omega\tau_2} + \dots \quad (2)$$

where $g_1, g_2, \dots, \tau_1, \tau_2, \dots$ are non-negative constants, and R_{∞} is the high-frequency resistance, or more generally as the continuous superposition of infinite Voigt processes as [18]:

$$Z(j\omega) = R_{\infty} + \int_0^{\infty} \frac{g(\tau)}{1 + j\omega\tau} d\tau \quad (3)$$

where $g(\tau) \geq 0$ is the classical DRT function. The Voigt model described by $\ker(j\omega, \tau) = (1 + j\omega\tau)^{-1}$ corresponds in the time domain to the response function $\phi(t)$ as $\phi(t) = \mathcal{L}^{-1}\{k_D(s); t\} = \tau^{-1}e^{-t/\tau}$, which has the rate $\Psi(t) = -d\phi(t)/dt = e^{-t/\tau}$ [19].

Plotting $g(\tau)$ vs. τ reveals the contribution of each relaxation timescale to the total impedance response: sharp peaks identify well-separated processes, whereas broad features indicate the presence of distributed dynamics [6, 16, 18, 20]. However, recovering $g(\tau)$ from a finite set of noisy or incomplete measurements $\{Z(j\omega_k)\}_{k=1}^N$ is an ill-posed inverse problem that requires some sort of regularization methods [13, 20–24], which

* aallagui@sharjah.ac.ae

[†] Also at Center for Advanced Materials Research, Research Institute of Sciences and Engineering, University of Sharjah, Sharjah 27272, United Arab Emirates

can significantly distort the recovered DRT [18]. Additionally, there is a fundamental limitation of the standard DRT model based on the Voigt kernel, which implies that the impedance tends toward a finite real value at the limit of very low frequencies [25]. This does not align well with the physics of systems featuring blocking electrodes, such as batteries and supercapacitors, for which the impedance approaches infinity as the frequency approaches zero due to charge accumulation or diffusion limitations [25, 26]. From a mathematical perspective, the DRT is often not well-defined for blocking systems because the imaginary component of the impedance must be integrable for a classical DRT deconvolution, which is not the case for systems exhibiting power-law tails [26].

This led to the introduction of the distribution of diffusion times (DDT) by Song and Bazant [26] to model the admittance rather than impedance of the system to effectively handle the non-integrable low-frequency behaviors. This translates the problem given by Eq. 1 from an impedance-based DRT framework to an admittance-based formulation [26]:

$$Y(j\omega) = Z^{-1}(j\omega) = \int_0^{\infty} \ker(j\omega, \tau) p(\tau) d\tau \quad (4)$$

where the (diffusion) kernel function can be for instance $\ker(j\omega, \tau) = (\coth(\sqrt{j\omega\tau})/\sqrt{j\omega\tau})^{-1}$ for planar blocking conditions, or $\ker(j\omega, \tau) = (\tanh(\sqrt{j\omega\tau})/\sqrt{j\omega\tau})^{-1}$ for planar transmissive conditions, or others based on the boundary conditions and the symmetry of the system under consideration [26]. This framework is considered mathematically and physically to be more appropriate for describing low-frequency diffusion impedance features [26]. In the same sense, the distribution of capacitive times (DCT) was introduced to accommodate unbounded low-frequency impedances as [20, 25]:

$$Y(j\omega) = G_0 + \int_0^{\infty} \frac{f(\tau)}{1 + (j\omega\tau)^{-1}} d\tau \quad (5)$$

where the kernel is now $\ker(j\omega, \tau) = (1 + (j\omega\tau)^{-1})^{-1}$. Both the DDP and DCT approaches allow to map distributions to different circuit topologies from the RC circuit used in the classical DRT structure.

Other extensions to the EIS inversion problem include the work of Allagui and Elwakil [27], wherein the Voigt kernel in Eq. 3 is replaced with the Davidson-Cole (DC) model, i.e. $\ker(j\omega, \tau) = (1 + (j\omega\tau))^{-\beta}$, or the work of Florsch, Revil, and Camerlynck [28], wherein the Havrilliak-Negami (HN) model is used instead, i.e. $\ker(j\omega, \tau) = (1 + (j\omega\tau)^\alpha)^{-\beta}$. This implies that if it is known that the macroscopic system is made of self-similar character at a microscopic level exhibiting a DC or a HN type of response, then the resulting distribution based on these kernels should exhibit lower complexity.

The motivation for the present work is the observation that both Eqs. 1 or 4 have a precise mathematical structure that has not been previously exploited in the literature. In all aforementioned cases, the kernels $(1 +$

$j\omega\tau)^{-1}$, $(1 + (j\omega\tau)^{-1})^{-1}$, $(1 + (j\omega\tau))^{-\beta}$, $(1 + (j\omega\tau)^\alpha)^{-\beta}$, $\coth(\sqrt{j\omega\tau})/\sqrt{j\omega\tau}$ and others [13, 26, 29] used for modeling the impedance or admittance (i.e. immittance) depend on the product $\omega\tau$, and the desired distribution function (i.e. DRT $g(\tau)$, DCT $f(\tau)$ or DDT $p(\tau)$) depends on τ alone. This is the hallmark of a Mellin convolution integral, for which the natural spectral tool is the Mellin transform. We show in this study how to convert the immittance inversion procedure into an exact algebraic relation in Mellin space (Section II). We validate the procedure analytically on a few examples of known impedance and admittance functions, including the constant phase element (CPE) and the Davidson-Cole (DC) model for both DRT and DCT recovery, and the finite-length Warburg with blocking boundary conditions as a DDT problem (Section III). We also present the numerical implementation of the immittance inversion procedure for the DRT and DCT of both the CPE and the DC model based on the fast Mellin transform (FMT) using the fast Fourier transform (FFT) algorithm (Section IV).

II. MELLIN TRANSFORM FORMULATION

The Mellin transform of a function $f(t)$, defined on the positive real axis $0 < t < \infty$, is defined as [30–32]:

$$\mathcal{M}\{f(t); s\} = \tilde{f}(s) = \int_0^{\infty} t^{s-1} f(t) dt \quad (6)$$

and the inverse is defined as:

$$f(t) = \mathcal{M}^{-1}\{\tilde{f}(s); t\} = \frac{1}{2\pi j} \int_{\sigma-j\infty}^{\sigma+j\infty} \tilde{f}(s) t^{-s} ds \quad (7)$$

where s is a complex variable, and the Bromwich contour $\Re(s) = \sigma$ must lie within the fundamental strip of analyticity of $\tilde{f}(s)$. The Mellin transform can be expressed in terms of the two-sided Laplace transform by making the change of variable $t = e^{-x}$, which gives [32]:

$$\mathcal{M}\{f(t); s\} = \mathcal{L}\{f(e^{-x}); s\} \quad (8)$$

The two-sided Laplace transform is defined as:

$$\mathcal{L}\{g(x); s\} = \int_{-\infty}^{\infty} g(x) e^{-sx} dx \quad (9)$$

Additionally, if we write $s = \sigma + j\omega$, we obtain [32]:

$$\mathcal{M}\{f(t); \sigma + j\omega\} = \mathcal{F}\{e^{-\sigma x} f(e^{-x}); \xi\} \quad (10)$$

where the Fourier transform is defined as:

$$\mathcal{F}\{f(x); \xi\} = \int_{-\infty}^{\infty} f(x) e^{-j\xi x} dx \quad (11)$$

The Mellin transform has many interesting properties that can be found in Erdélyi et al. [30], but the key property for the present work is the Mellin (generalized or

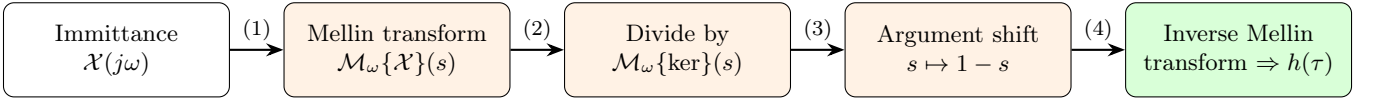


FIG. 1. Flowchart of the Mellin-based immittance inversion procedure. The measured immittance $\mathcal{X}(j\omega)$ (impedance $Z(j\omega)$ or admittance $Y(j\omega)$) is mapped to its corresponding distribution function $h(\tau)$ via four steps in Mellin space. The kernel $\ker(j\omega, \tau)$ is chosen according to the framework of interest: Voigt for DRT, capacitive for DCT, or diffusion-based for DDT.

multiplicative [31]) convolution theorem. For an integral of the form [30]:

$$h(t) = t^a \int_0^\infty \xi^\beta f_1(t\xi) f_2(\xi) d\xi \quad (12)$$

the Mellin transform is given by:

$$\tilde{h}(s) = \tilde{f}_1(s+a)\tilde{f}_2(1-s-a+\beta) \quad (13)$$

which converts the Mellin convolutions into point-wise products in the s domain, exactly as the Fourier convolution theorem converts ordinary convolutions into products in the frequency domain. Comparing with Eqs. 1 or 4, the Mellin transform of an immittance function $\mathcal{X}_r(j\omega)$ is given by:

$$\mathcal{M}_\omega\{\mathcal{X}_r(j\omega); s\} = \mathcal{M}_\omega\{\ker(j\omega); s\}\mathcal{M}_\tau\{g(\tau); 1-s\} \quad (14)$$

from which we obtained the main result of this study:

$$\mathcal{M}_\tau\{g(\tau); s\} = \frac{\mathcal{M}_\omega\{\mathcal{X}_r(j\omega); 1-s\}}{\mathcal{M}_\omega\{\ker(j\omega); 1-s\}} \quad (15)$$

after substituting $s \mapsto 1-s$. We remark the analogy that a transfer function of a linear system is obtained as the ratio of output to input spectra in Fourier space. Here the Mellin transform of the distribution function $g(\tau)$ is obtained as the ratio of the immittance spectrum to the kernel spectrum in Mellin space. The distribution $g(\tau)$ in the τ domain is then recovered by Mellin inversion of Eq. 15. Fig. 1 provides a flowchart summary of the proposed Mellin-based immittance inversion procedure.

We note that the exact inversion formula in Eq. 15 require no regularization at the analytical level. In practical implementations with numerical data, however, the Mellin integrals are evaluated over a finite frequency window, and usually in the presence of noise. This necessitates spectral truncation and/or windowing in Mellin space, which act as implicit regularization themselves [32–35] (see Section IV).

III. ANALYTICAL EXAMPLES

A. Distribution of relaxation times

As a first example to validate the inversion procedure, we consider the reduced impedance function defined from

Eq. 3 with the removal of the R_∞ offset in the DRT sense as:

$$\mathcal{X}_r(j\omega) = Z_r(j\omega) = Z(j\omega) - R_\infty = \int_0^\infty \frac{g(\tau)}{1+j\omega\tau} d\tau \quad (16)$$

This is clearly a Mellin convolution of the DRT function $g(\tau)$ with the basis function $(1+j\omega\tau)^{-1}$ (Voigt model). Taking the Mellin transform of $Z_r(j\omega)$ with respect to the variable ω gives:

$$\mathcal{M}_\omega\{Z_r(j\omega); s\} = \pi(j)^{-s} \csc(\pi s) \mathcal{M}_\tau\{g(\tau); 1-s\} \quad (17)$$

where we used the result [30]:

$$\mathcal{M}\{(1+at)^{-\nu}; s\} = a^{-s} B(s, \nu-s), \quad 0 < \text{Re}(s) < \text{Re}(\nu) \quad (18)$$

For $\nu = 1$, the Mellin transform of the Voigt kernel with respect ω simplifies to:

$$\mathcal{M}_\omega\{(1+j\omega\tau)^{-1}; s\} = \pi(j\tau)^{-s} \csc(\pi s), \quad 0 < \text{Re}(s) < 1 \quad (19)$$

The strip $0 < \Re(s) < 1$ is the fundamental strip of the Voigt kernel's Mellin transform, and therefore the inversion contour $\Re(s) = \sigma$ must lie within this strip. Note that the Mellin argument shift from s to $1-s$ in Eq. 17 absorbs the term τ^{-s} that comes from Eq. 19. Solving for the DRT, we obtain:

$$\mathcal{M}_\tau\{g(\tau); 1-s\} = \pi^{-1} \sin(\pi s) (j)^s \mathcal{M}_\omega\{Z_r(j\omega); s\} \quad (20)$$

and then with $1-s \mapsto s$ we obtain:

$$\mathcal{M}_\tau\{g(\tau); s\} = \pi^{-1} \sin(\pi(1-s)) (j)^{1-s} \mathcal{M}_\omega\{Z_r(j\omega); 1-s\} \quad (21)$$

The DRT function $g(\tau)$ is recovered from by Mellin inversion (Fig. 1). The relations given by Eqs. 17, 19 and thus Eq. 21 are exact, and holds for any admissible impedance function.

We apply the procedure above to the case of the CPE, whose impedance is defined as [36]:

$$Z_c(j\omega) = R_0(j\omega\tau_c)^{-\alpha} = \int_0^\infty \frac{g_c(\tau)}{1+j\omega\tau} d\tau \quad (22)$$

where $0 < \alpha < 1$, R_0 is the resistance, and τ_c is a characteristic time constant. Its Mellin transform is:

$$\mathcal{M}_\omega\{Z_c(j\omega); s\} = 2\pi R_0(j\tau_c)^{-\alpha} \delta(s-\alpha) \quad (23)$$

and therefore

$$\mathcal{M}_\tau\{g(\tau); (1-s)\} = 2R_0\tau_c^{-\alpha} j^{s-\alpha} \sin(\pi s) \delta(s-\alpha) \quad (24)$$

which we then rewrite as:

$$\mathcal{M}_\tau\{g(\tau); s\} = 2R_0\tau_c^{-\alpha} j^{1-\alpha-s} \sin(\pi s) \delta(s - (1 - \alpha)) \quad (25)$$

noting that $\sin(\pi(1 - s)) = \sin(\pi s)$. The inverse Mellin transform with $s = c + j\xi$ for $\xi \in]-\infty; \infty[$ ($ds = j d\xi$), and $c = 1 - \alpha$, is:

$$\begin{aligned} g_c(\tau) &= \frac{1}{2\pi j} \int_{c-j\infty}^{c+j\infty} 2R_0\tau_c^{-\alpha} j^{1-\alpha-s} \sin(\pi s) \delta(s - (1 - \alpha)) \tau^{-s} ds \\ &= \frac{1}{2\pi} \int_{-\infty}^{+\infty} 2R_0\tau_c^{-\alpha} j^{1-\alpha-s} \sin(\pi s) \delta(\xi) \tau^{-s} d\xi \end{aligned} \quad (26)$$

where we used $\delta(s - (1 - \alpha)) = \delta(j\xi) = \delta(\xi)/|j| = \delta(\xi)$. With the use of the translation property of the Dirac delta function $\int_{-\infty}^{\infty} f(t)\delta(t - T)dt = f(T)$, i.e. with the evaluation at $s = 1 - \alpha$, we obtain the well-known power law in τ [27, 36]

$$g_c(\tau) = \pi^{-1} R_0 \sin(\pi\alpha) \tau_c^{-\alpha} \tau^{\alpha-1} \quad (27)$$

Note that $g_c(\tau) > 0$ for all $\tau > 0$, which is consistent with the physical requirement that the DRT be non-negative. The integral $\int_0^{\infty} g_c(\tau) d\tau$ diverges, which is in line with the absence of a characteristic relaxation timescale in the CPE.

We apply the same procedure again to the case of the DC impedance given by [37]:

$$Z_d(j\omega) = \frac{R_0}{(1 + j\tau_0\omega)^\alpha} \quad (28)$$

Its Mellin transform with respect to ω is [30]:

$$\mathcal{M}_\omega\{Z_d(j\omega); s\} = R_0 \frac{\Gamma(s)\Gamma(\alpha - s)}{(j\tau_0)^s \Gamma(\alpha)} \quad (29)$$

which is analytic for $0 < \Re(s) < \alpha$ (this is the fundamental strip of the DC impedance's Mellin transform), and therefore $\mathcal{M}_\tau\{g_d(\tau); s\}$ is obtained after substituting $s \mapsto 1 - s$ as:

$$\mathcal{M}_\tau\{g_d(\tau); s\} = R_0(\tau_0)^{s-1} \frac{\Gamma(s + \alpha - 1)}{\Gamma(\alpha)\Gamma(s)} \quad (30)$$

Applying the inverse Mellin transform with respect to τ gives the expected result [27, 36]:

$$\begin{aligned} g_d(\tau) &= \frac{R_0 \sin(\alpha\pi)}{\pi\tau(\tau_0/\tau - 1)^\alpha}, \quad \tau < \tau_0 \\ &= 0, \quad \text{otherwise} \end{aligned} \quad (31)$$

We verify that in this case:

$$\int_0^{\infty} g_d(\tau) d\tau = R_0 \quad (32)$$

B. Distribution of capacitive times

We now apply the DCT framework to the CPE admittance, which is defined as:

$$Y_c(j\omega) = R_0^{-1} (j\omega\tau_c)^\alpha = \int_0^{\infty} \frac{f_c(\tau)}{1 + (j\omega\tau)^{-1}} d\tau \quad (33)$$

Its Mellin transform is:

$$\mathcal{M}_\omega\{Y_c(j\omega); s\} = 2\pi R_0^{-1} (j\tau_c)^\alpha \delta(s + \alpha) \quad (34)$$

and that of the DCT kernel is:

$$\mathcal{M}_\omega\{(1 + (j\omega\tau)^{-1})^{-1}; s\} = -\pi(j\tau)^{-s} \csc(\pi s) \quad (35)$$

with $-1 < \Re(s) < 0$, so the inversion contour for the DCT must satisfy $-1 < \Re(s) < 0$. Then

$$\mathcal{M}_\tau\{f_c(\tau)\}(1 - s) = -2R_0^{-1} (j\tau_c)^\alpha (j)^s \sin(\pi s) \delta(s + \alpha) \quad (36)$$

Evaluating the delta function at $s = -\alpha$ gives:

$$\mathcal{M}_\tau\{f_c(\tau)\}(1 - s) = 2R_0^{-1} \tau_c^\alpha \sin(\pi\alpha) \delta(s + \alpha) \quad (37)$$

Applying the argument shift $s \mapsto 1 - s$:

$$\mathcal{M}_\tau\{f_c(\tau)\}(s) = 2R_0^{-1} \tau_c^\alpha \sin(\pi\alpha) \delta(s - (1 + \alpha)) \quad (38)$$

Applying the inverse Mellin transform on the Bromwich contour $c = 1 + \alpha$, with $s = (1 + \alpha) + j\xi$ and $ds = j d\xi$:

$$\begin{aligned} f_c(\tau) &= \frac{1}{2\pi j} \int_{c-j\infty}^{c+j\infty} 2R_0^{-1} \tau_c^\alpha \sin(\pi\alpha) \delta(s - (1 + \alpha)) \tau^{-s} ds \\ &= \frac{1}{2\pi} \int_{-\infty}^{+\infty} 2R_0^{-1} \tau_c^\alpha \sin(\pi\alpha) \delta(\xi) \tau^{-s} d\xi \end{aligned} \quad (39)$$

Applying the sifting property of $\delta(\xi)$ at $\xi = 0$, i.e. $s = 1 + \alpha$, results in :

$$f_c(\tau) = \pi^{-1} R_0^{-1} \sin(\pi\alpha) \tau_c^\alpha \tau^{-(1+\alpha)} \quad (40)$$

which is also a pure power law in τ . As in the DRT case, the integral $\int_0^{\infty} f_c(\tau) d\tau$ also diverges.

As a second example, we consider the reduced admittance given by the inverse of the DC impedance in Eq 28, i.e.:

$$Z_d^{-1}(j\omega) = R_0^{-1} (1 + j\tau_0\omega)^\alpha = \int_0^{\infty} \frac{f_d(\tau)}{1 + (j\omega\tau)^{-1}} d\tau \quad (41)$$

With:

$$\mathcal{M}_\omega\{(1 + (j\omega\tau)^{-1})^{-1}; s\} = -\pi(j\tau)^{-s} \csc(\pi s) \quad (42)$$

and

$$\mathcal{M}_\omega\{Z_d^{-1}(j\omega); s\} = \frac{\Gamma(s)\Gamma(-\alpha - s)}{R_0(j\tau_0)^s \Gamma(-\alpha)} \quad (43)$$

we obtain the corresponding Mellin-transformed DCT as:

$$\mathcal{M}_\tau \{f_d(\tau); s\} = -R_0^{-1}(\tau_0)^{s-1} \frac{\Gamma(s-\alpha-1)}{\Gamma(-\alpha)\Gamma(s)} \quad (44)$$

The inverse Mellin transform with respect to τ gives:

$$\begin{aligned} f_d(\tau) &= \frac{(\tau_0/\tau - 1)^\alpha \sin(\alpha\pi)}{\pi R_0 \tau}, \quad \tau < \tau_0 \\ &= 0, \quad \text{otherwise} \end{aligned} \quad (45)$$

Unlike the DRT case, the integral $\int_0^\infty f_d(\tau) d\tau$ diverges, which is consistent with the unbounded low-frequency behavior of the DC admittance.

C. Distribution of diffusion times

We consider here the simple case of finite-length Warburg admittance of a planar electrode system with blocking boundary conditions, defined as [26]:

$$\begin{aligned} Y_w(j\omega) &= \left(R_0 \frac{\coth(\sqrt{j\omega\tau_0})}{\sqrt{j\omega\tau_0}} \right)^{-1} \\ &= \int_0^\infty \left(\frac{\coth(\sqrt{j\omega\tau})}{\sqrt{j\omega\tau}} \right)^{-1} p(\tau) d\tau \end{aligned} \quad (46)$$

where the DDT function $p(\tau)$ is to be determined [26]. This problem represents a single blocking diffusion element, which should give immediately $p(\tau) = R_0^{-1} \delta(\tau - \tau_0)$ (sifting property of the delta function), that we verify below based on our theory.

First, for the Mellin transform of the kernel given by $\ker_w(j\omega, \tau) = \sqrt{j\omega\tau} \tanh(\sqrt{j\omega\tau})$, we have after the substitutions $u = \sqrt{j\omega\tau}$, $\omega = u^2/(j\tau)$, $d\omega = 2u du/(j\tau)$:

$$\mathcal{M}_\omega \{\ker_w(j\omega, \tau); s\} = \frac{2}{(j\tau)^s} \int_0^\infty u^{2s} \tanh(u) du \quad (47)$$

We now substitute with the series representation of $\tanh(z)$ given by [38]

$$\tanh(z) = 8z \sum_{k=1}^\infty \frac{1}{\pi^2(2k-1)^2 + 4z^2}, \quad \frac{iz}{\pi} - \frac{1}{2} \notin \mathbb{Z} \quad (48)$$

to obtain:

$$\int_0^\infty u^{2s} \tanh(u) du = \sum_{k=1}^\infty \int_0^\infty \frac{2u^{2s+1}}{u^2 + (k-1/2)^2 \pi^2} du \quad (49)$$

$$= - \sum_{k=1}^\infty \pi^{2s+1} (k-1/2)^{2s} \csc(\pi s) \quad (50)$$

$$= -\pi^{2s+1} \csc(\pi s) \sum_{k=1}^\infty (k-1/2)^{2s} \quad (51)$$

$$= \pi^{2s+1} \csc(\pi s) (1-4^{-s}) \zeta(-2s) \quad (52)$$

where $\zeta(z) = \sum_{k=1}^\infty k^{-z}$ is the Riemann zeta function. Substituting back into Eq. 47 gives:

$$\mathcal{M}_\omega \{\ker_w(j\omega, \tau); s\} = \frac{2\pi^{2s+1}(1-4^{-s})\zeta(-2s)}{(j\tau)^s \sin(\pi s)} \quad (53)$$

It is worth noting that this result is not a classical Mellin transform in the strict sense, since the kernel $\ker_w(j\omega, \tau) = \sqrt{j\omega\tau} \tanh(\sqrt{j\omega\tau})$ grows as $\sqrt{j\omega\tau}$ as $\omega \rightarrow \infty$, and therefore the defining integral diverges at the upper limit for any $\text{Re}(s) > 0$. The result is thus understood in the sense of analytic continuation.

Second, since $Y_w(j\omega) = R_0^{-1} \ker_w(j\omega, \tau_0)$, we replace $\tau \rightarrow \tau_0$ in Eq. 53 to obtain:

$$\mathcal{M}_\omega \{Y_w(j\omega); s\} = \frac{2\pi^{2s+1}(1-4^{-s})\zeta(-2s)}{R_0(j\tau_0)^s \sin(\pi s)} \quad (54)$$

Now solving for $\mathcal{M}_\tau \{p\}(1-s)$ by making sure the term τ^{-s} is properly accounted for when the argument is shifted from s to $1-s$ as done above, gives $\mathcal{M}_\tau \{p(\tau); 1-s\} = \tau_0^{-s}/R_0$, and thus

$$\mathcal{M}_\tau \{p(\tau); s\} = R_0^{-1} \tau_0^{s-1} \quad (55)$$

The inverse Mellin transform gives, as expected, a delta function concentrated at τ_0 :

$$p(\tau) = R_0^{-1} \delta(\tau - \tau_0) \quad (56)$$

The normalization is also verified from $\int_0^\infty p(\tau) d\tau = R_0^{-1}$. Eq. 56 means again that the system is characterized by a single diffusion time scale $\tau_0 = L^2/D$ (L is the diffusion length and D the diffusion coefficient). This is the analog of the DRT of a simple RC circuit, which is also a single delta function concentrated at the time constant $\tau_0 = RC$.

IV. NUMERICAL IMPLEMENTATION

In this section, we present examples of numerical implementation of the Mellin transform-based procedure of Fig. 1 for both the CPE and DC model. We describe the Fast Mellin Transform (FMT) implementation on a logarithmic frequency grid using the standard FFT algorithm [35].

A. Mellin-FFT Inversion Algorithm

The whole numerical procedure is summarized in Algorithm 1. With the change of variable $\omega = e^{-x}$ and with $s = \sigma + j\xi$, we can write the Mellin transform of the immittance function $\mathcal{X}_r(j\omega)$ in Eq. 14 in a Fourier-transform form as [33]:

$$\mathcal{M}_\omega \{\mathcal{X}_r(j\omega); \sigma + j\xi\} = \mathcal{F}\{e^{-\sigma x} \mathcal{X}_r(je^{-x}); \xi\} \quad (57)$$

Numerically, this consists of first discretizing the x -axis, such that $x_n = -L + n \Delta x$ for $n = 0, \dots, N-1$ ($\Delta x =$

$2L/N$). The sampled angular frequencies are therefore $\omega_n = e^{-x_n}$ (Steps 1 and 2 in Algorithm 1). The forward Mellin transform is then computed by FFT through:

$$\tilde{X}(\sigma + j\xi_k) = \Delta x e^{-j\xi_k x_0} \text{FFT}\{e^{-\sigma x_n} X(je^{-x_n})\}_k \quad (58)$$

with $x_0 = -L$ and ξ_k are the discrete Fourier frequency bins ($\xi_k = k/(N \Delta x)$, $k = 0, 1, \dots, N/2 - 1, -N/2, \dots, -1$) (Step 3). The phase factor $e^{-j\xi_k x_0}$ is essential as it compensates for the fact that the FFT assumes samples starting at $x = 0$, while the actual grid starts at $x = -L$. This is then followed by the argument shift $s \mapsto 1 - s$, which is implemented by an index reflection in the Mellin-frequency array (Step 4).

Next, the division given by Eq. 15 is numerically ill-posed and requires stabilization. Because the kernel is conjugate-symmetric on the contour, we therefore restrict the division to the better-conditioned half to avoid having unstable noise from the high $|\xi|$ tail. We also adopt a Tikhonov-regularized division (with parameter λ) to obtain:

$$\tilde{h}_\lambda(s) = \frac{\tilde{\mathcal{X}}_r(1-s)\tilde{\text{ker}}(1-s)^*}{|\tilde{\text{ker}}(1-s)|^2 + \lambda} \quad (59)$$

which is then multiplied by a Hann window:

$$W(\xi) = \frac{1}{2} \left[1 + \cos \left(\frac{\pi \xi}{\xi_{\text{cut}}} \right) \right] \quad (60)$$

to suppress Gibbs type oscillations. Together they act as a low-pass denoising filter (Step 6).

Then, because the desired distribution function is real-values, its Mellin-domain transform satisfies the conjugate symmetry. This is what is implemented in Algorithm 1 under Step 7, Hermitian completion.

After assembling the stabilized Mellin-domain spectrum, the inverse Mellin transform back to the τ -domain at $\tau = e^{-y}$ is obtained via:

$$h_n = e^{\sigma_h x_n} \text{Re} \left[\Delta x^{-1} \text{IFFT} \left\{ \tilde{h}(\xi_k) e^{j\xi_k x_0} \right\}_n \right] \quad (61)$$

The phase factor $e^{j\xi_k x_0}$ is the inverse counterpart of the phase factor used in the forward transform.

A critical step for successful inversion is the choice of the Mellin abscissa σ_h for the inverse transform. This must lie within the fundamental strip of the distribution function's Mellin transform. For the CPE DRT, the relevant Mellin pole is at $s = \alpha$, so the natural choice is $\sigma_h = 1 - \alpha$ (we use $\sigma_h = 0.25$ for $\alpha = 0.75$). For the CPE DCT, the pole is at $s = -\alpha$, giving $\sigma_h = 1 + \alpha$ (we use $\sigma_h = 1.75$). For the DC model, whose DRT has a strip of analyticity $0 < \Re(s) < \alpha$, the centre of the strip gives $\sigma_h = 1 - \alpha/2$ (we use $\sigma_h = 0.75$ for $\alpha = 0.5$). In general, σ_h can be determined adaptively from the high- and low-frequency power-law exponents of the measured immittance, without prior knowledge of the underlying physical model.

Algorithm 1 Mellin-FFT inversion

Require: Immittance data $\{(\omega_n, X(j\omega_n))\}_{n=0}^{N-1}$, regularisation parameter λ , cutoff ξ_{cut} , Mellin abscissa ρ , half-width L , step Δx

- 1: **Step 1: Build grids**
- 2: Construct log-frequency grid:

$$x_n = -L + n \Delta x, \quad n = 0, \dots, N - 1$$

- 3: Construct Mellin-frequency grid:

$$\{\xi_k\} = 2\pi \text{fftfreq}(N, \Delta x)$$

- 4: **Step 2: Evaluate immittance on the grid**
- 5: Set $\omega_n = e^{-x_n}$ and evaluate immittance at each grid point
- 6: **Step 3: Forward FMT at abscissa $\sigma = \rho$**
- 7: Compute FFT and apply phase correction and scaling:

$$\tilde{X}_k = \Delta x e^{-j\xi_k x_0} \text{FFT}\{e^{-\sigma x_n} X(j\omega_n)\}_k$$

- 8: **Step 4: Argument reflection**
- 9: Map spectrum to the reflected contour $s \mapsto 1 - s$:

$$\tilde{X}_k^{(1-s)} = \tilde{X}_{-k \bmod N}$$

- 10: **Step 5: Evaluate Mellin kernel on the reflected contour**

- 11: Set $q_k = \sigma - j\xi_k$ and compute the kernel transform:

$$\tilde{K}_k = \frac{\pi e^{-j\pi q_k/2}}{\sin(\pi q_k)}$$

(use the Voigt kernel as written, or its negative for the capacitive kernel)

- 12: **Step 6: Stabilized algebraic inversion on the stable half $\xi_k \in [-\xi_{\text{cut}}, 0]$**
- 13: Apply Tikhonov regularization with Hann windowing:

$$\tilde{h}_k = \tilde{X}_k^{(1-s)} \tilde{K}_k^* \left(|\tilde{K}_k|^2 + \lambda \right)^{-1} W_k, \quad W_k = \frac{1}{2} [1 + \cos(\pi \xi_k / \xi_{\text{cut}})]$$

- 14: **Step 7: Hermitian completion**

- 15: For every k on the stable side set $\tilde{h}_{-k \bmod N} \leftarrow \tilde{h}_k^*$; force $\tilde{h}_0 \in \mathbb{R}$

- 16: **Step 8: Inverse FMT at abscissa $\sigma_h = 1 - \rho$**

- 17: Apply phase correction and compute IFFT, then rescale:

$$h_n = e^{\sigma_h x_n} \text{Re} \left[\Delta x^{-1} \text{IFFT} \left\{ \tilde{h}_k e^{j\xi_k x_0} \right\}_n \right]$$

- 18: **Step 9: Optional positivity clip**

- 19: $h_n \leftarrow \max(h_n, 0)$

- 20: **return** $\{(e^{-x_n}, h_n)\}_{n=0}^{N-1}$
-

B. CPE model DRT and DCT recovery

Fig. 2 shows the Nyquist plot of $Z_c(j\omega) = R_0(j\omega\tau_c)^{-\alpha}$ for $R_0 = 1 \Omega$, $\tau_c = 1 \text{ s}$, $\alpha = 0.75$ (clean CPE), as well as noisy data generated using [39]:

$$Z_m(j\omega_k) = Z_c(j\omega_k) [1 + \sigma \varepsilon_{R,k} + j\sigma \varepsilon_{I,k}] \quad (62)$$

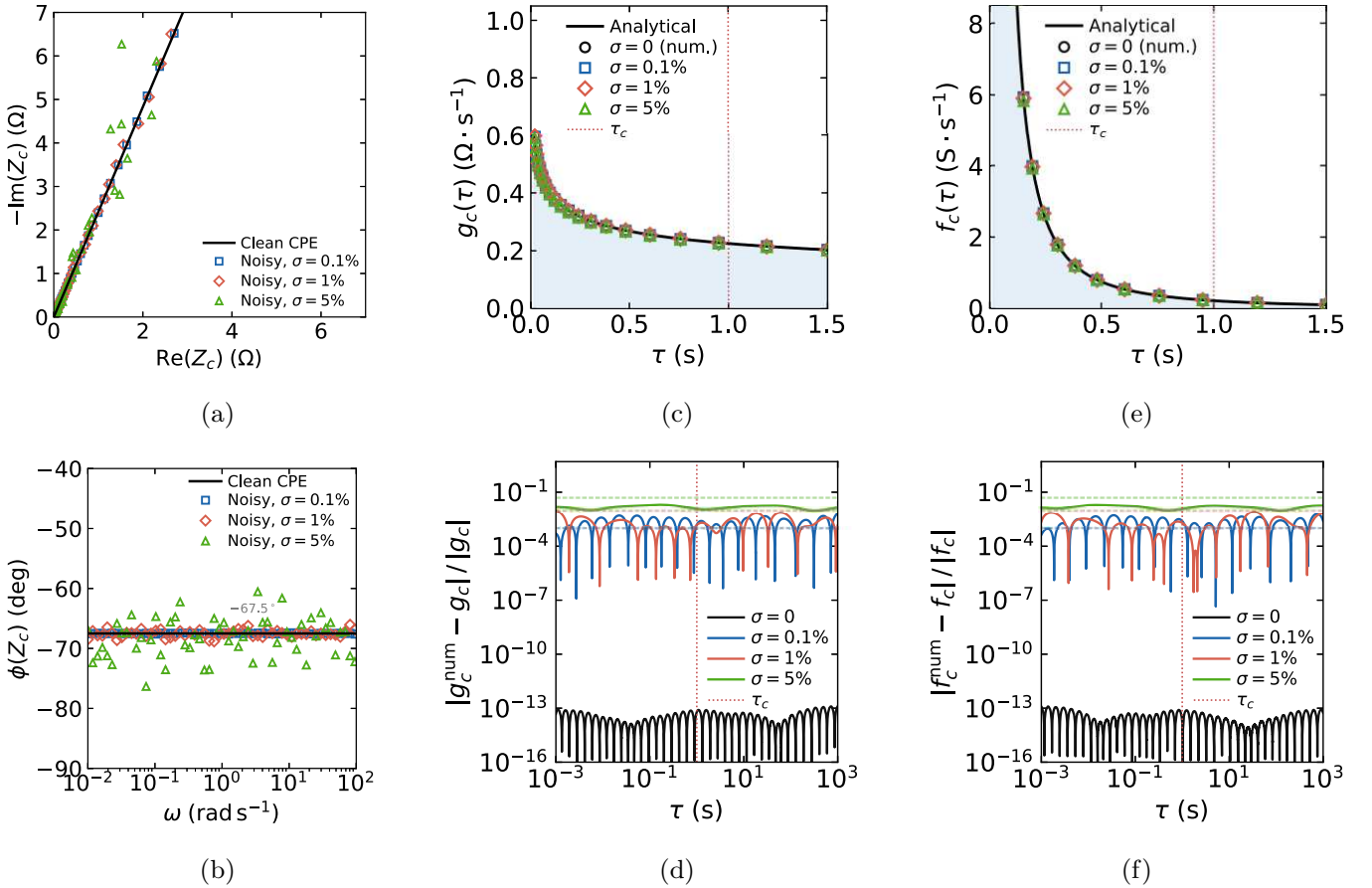


FIG. 2. Numerical results for the CPE (of impedance $Z_c(j\omega) = R_0(j\omega\tau_c)^{-\alpha}$) with $R_0 = 1 \Omega$, $\tau_c = 1 \text{ s}$, $\alpha = 0.75$, and noise levels $\sigma \in \{0, 0.1\%, 1\%, 5\%\}$. **(a)** Nyquist plot of $Z_c(j\omega)$: the clean CPE (solid black) traces a straightline at -67.5° ; markers show the noisy data. **(b)** corresponding Bode phase vs. ω (log scale). **(c)** DRT $g_c(\tau)$ recovery on linear axes: solid black curve is the analytical Eq. (27); markers are the Mellin-FFT recovery including the noise-free case ($\sigma = 0$). Red dotted line marks $\tau_c = 1 \text{ s}$. **(d)** Pointwise relative error of the DRT recovery; dashed horizontal lines mark the input noise level σ . The $\sigma = 0$ curve stays near 10^{-14} . **(e)** DCT $f_c(\tau)$ recovery; same conventions as (c). **(f)** Pointwise relative error of the DCT recovery; same conventions as (d).

where $\varepsilon_{R,k}, \varepsilon_{I,k} \sim \mathcal{N}(0, 1)$, and $\sigma \in \{0, 0.1\%, 1\%, 5\%\}$. Fig. 2(a) shows the Nyquist plot, where the clean CPE traces an inclined straight line at -67.5° . This can be clearly seen from the Bode phase plot in Fig. 2(b). The recovered DRT and DCT are shown in Fig. 2(c) and Fig. 2(e) for all noise levels, with the corresponding errors in Figs. 2(d) and 2(f).

For the noise-free case ($\sigma = 0$), we set $N = 2^{16}$, $L = 30$, $\sigma_{h,\text{DRT}} = 0.25$, $\sigma_{h,\text{DCT}} = 1.75$, and $\{\xi_{\text{cut}}, \lambda\} = \{10, 10^{-20}\}$. The recovered distribution attains a relative error of order 10^{-13} – 10^{-14} across twelve decades in τ , which is essentially the floating-point limit for double-precision FFT arithmetic with $N = 2^{16}$ samples. We note that the Tikhonov parameter λ and cutoff ξ_{cut} for the noisy cases were determined by minimising the L^2 relative error against the analytical reference distributions. For experimental data lacking an analytical reference, these can be tuned using standard regularisation selection criteria such as the L-curve or discrepancy prin-

ciple.

For the noisy data, we kept the same general parameters of the algorithm, but adjusted the stabilization parameters: $\{\sigma, \xi_{\text{cut}}, \lambda\} = \{0.1\%, 8, 10^{-4}\}$, $\{1\%, 6, 10^{-2}\}$, and $\{5\%, 4, 0.3\}$. The pointwise relative errors in Figs. 2(d) and 2(f) are practically flat across the six decades of the τ window, and lie below the input noise level σ at every τ tested (dashed horizontal lines), confirming that the Tikhonov-Hann stabilization acts as a useful low-pass denoising filter.

C. DC model DRT and DCT recovery

We now validate the inversion procedure numerically for the DC model. We use $R_0 = 1 \Omega$, $\tau_0 = 1 \text{ s}$, $\alpha = 0.5$. The DC impedance is $Z_d(j\omega) = R_0/(1 + j\tau_0\omega)^\alpha$ and the corresponding admittance is $Y_d(j\omega) = R_0^{-1}(1 + j\tau_0\omega)^\alpha$. The analytical DRT and DCT are given by Eqs. (31)

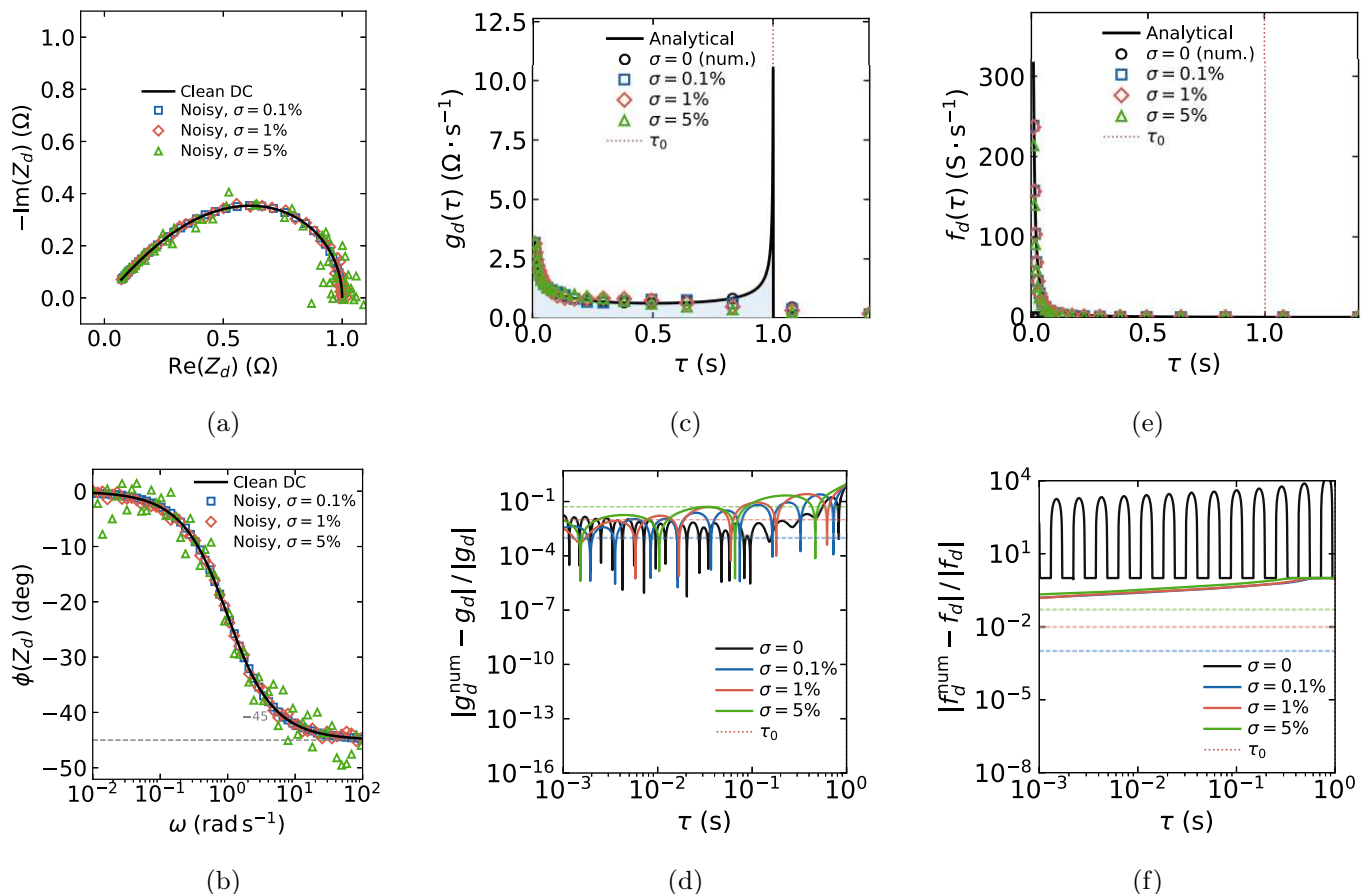


FIG. 3. Numerical results for the Davidson-Cole model (of impedance $Z_d(j\omega) = R_0(1 + j\tau_0\omega)^{-\alpha}$) with $R_0 = 1 \Omega$, $\tau_0 = 1 \text{ s}$, $\alpha = 0.5$, and noise levels $\sigma \in \{0, 0.1\%, 1\%, 5\%\}$. **(a)** Nyquist plot of $Z_d(j\omega_k)$: clean DC shows a depressed semi-arc (solid black), and open markers show the noisy data. **(b)** corresponding Bode phase vs. ω (log scale); the phase is frequency-dependent and approaches $-90\alpha = -45^\circ$ (dashed line) asymptotically at high frequency. **(c)** DRT $g_d(\tau)$ recovery on linear axes: solid black curve is the analytical Eq. (31); markers are the Mellin-FFT recovery including the noise-free case ($\sigma = 0$). **(d)** Pointwise relative error of the DRT recovery; dashed horizontal lines mark the input noise level σ . The error window is restricted to $\tau < \tau_0$ where the distribution is non-zero. **(e)** DCT $f_d(\tau)$ recovery; same conventions as (c). **(f)** Pointwise relative error of the DCT recovery; same conventions as (d); the noise-free error stays near 10^{-13} – 10^{-14}

and (45) respectively. The same multiplicative noise model as in Eq. (62) is used with $\sigma \in \{0, 0.1\%, 1\%, 5\%\}$. The DC DRT Mellin transform has fundamental strip $0 < \Re(s) < \alpha = 0.5$, so we choose the inversion abscissa at the centre of the strip, $\sigma_{h,\text{DRT}} = 1 - \alpha/2 = 0.75$. Similarly, for the DC DCT, the contour is placed at $\sigma_{h,\text{DCT}} = 1 + \alpha/2 = 1.25$. For the noise-free case, we use $\{\xi_{\text{cut}}, \lambda\} = \{12, 10^{-20}\}$; for the noisy cases, $\{\sigma, \xi_{\text{cut}}, \lambda\} = \{0.1\%, 9, 10^{-4}\}$, $\{1\%, 7, 10^{-2}\}$, $\{5\%, 5, 0.2\}$.

The results are shown in Fig. 3. Figs. 3(a) and 3(b) show the Nyquist plot and Bode phase of the DC impedance for $R_0 = 1 \Omega$, $\tau_0 = 1 \text{ s}$, $\alpha = 0.5$, along with noisy data with $\sigma \in \{0.1\%, 1\%, 5\%\}$. The Nyquist arc is a curved with $Z = R_0$ as $\omega \rightarrow 0$ and at $Z = 0$ as $\omega \rightarrow \infty$, and the Bode phase is frequency-dependent, approaching $-90\alpha = -45^\circ$ asymptotically. Figs. 3(c) and 3(e) show the DRT and DCT recovery on linear axes. The Mellin-FFT method reproduces the analytical distributions closely up to $\tau \approx \tau_0$, including the steep rise near

the truncation point $\tau_0 = 1 \text{ s}$ (marked by the red dotted line). The noise-free recovery ($\sigma = 0$) sits essentially on the analytical curve throughout the interval. At larger noise levels, the recovered distributions deviate primarily near the singularity at τ_0 , where the regularization smooths the sharp endpoint. The pointwise relative errors in Figs. 3(d) and 3(f) confirm that the error remains below the input noise level σ over most of the τ window, and lies near the floating-point limit ($\sim 10^{-13}$) for the noise-free case.

V. CONCLUSION

We have shown that the distribution of relaxation times (DRT), the distribution of capacitive times (DCT), and the distribution of diffusion times (DDT) problems all admit an exact Mellin-domain formulation valid for arbitrary immittance functions. The key observation is

that all standard immittance kernels depend on the product $\omega\tau$ rather than on ω and τ independently, which is precisely the hallmark of a Mellin convolution. This structure, which has not been previously exploited in the EIS literature, makes the Mellin transform the most natural spectral framework for immittance inversion. The inversion problem is then reduced to algebraic operations in Mellin space: the Mellin transform of the immittance is divided by the Mellin transform of the kernel, followed by an argument shift $s \mapsto 1 - s$, and then an inverse Mellin transform that leads to the desired distribution function (see Fig. 1). We verified the approach analytically on a few examples of impedance and admittance functions, including the CPE and the DC model for both DRT and DCT recovery, and the finite-length Warburg

admittance of a planar electrode with blocking boundary conditions for the DDT problem. Numerical validation using the fast Mellin transform via FFT was carried out for both the CPE and the DC model, covering DRT and DCT recovery under clean and noisy conditions (σ up to 5%). For the CPE, the noise-free error reaches the floating-point limit ($\sim 10^{-14}$), and for the DC model, the method recovers the distribution faithfully, with errors below the input noise level across most of the timescale window. Two practical limitations should be noted: (i) the method requires a sufficiently wide frequency window to capture the significant Mellin frequency content of the spectrum, and (ii) the inversion abscissa σ_h must be chosen to lie within the fundamental strip of the distribution's Mellin transform.

-
- [1] J. Huang, Y. Gao, J. Luo, S. Wang, C. Li, S. Chen, and J. Zhang, Editors' choice—review—impedance response of porous electrodes: theoretical framework, physical models and applications, *J. Electrochem. Soc.* **167**, 166503 (2020).
- [2] A. Lasia, *Electrochemical impedance spectroscopy and its applications* (Springer, 2014).
- [3] V. Vivier and M. E. Orazem, Impedance analysis of electrochemical systems, *Chem. Rev.* **122**, 11131 (2022).
- [4] S. Wang, J. Zhang, O. Gharbi, V. Vivier, M. Gao, and M. E. Orazem, Electrochemical impedance spectroscopy, *Nat. Rev. Methods Primers* **1**, 41 (2021).
- [5] A. C. Lazanas and M. I. Prodromidis, Electrochemical impedance spectroscopy—a tutorial, *ACS Measurement Science Au* **3**, 162 (2023).
- [6] B. A. Boukamp, Guidance to solid state electrochemical impedance spectroscopy, *Electrochim. Acta* **537**, 146892 (2025).
- [7] M. E. Orazem and B. Ulgut, The utility and limitations of distribution of relaxation times (drt) methods for impedance analysis, *J. Electrochem. Soc.* **172**, 073505 (2025).
- [8] Z. Lukács and T. Kristóf, A generalized model of the equivalent circuits in the electrochemical impedance spectroscopy, *Electrochim. Acta* **363**, 137199 (2020).
- [9] P. Jash, R. K. Parashar, C. Fontanesi, and P. C. Mondal, The importance of electrical impedance spectroscopy and equivalent circuit analysis on nanoscale molecular electronic devices, *Adv. Funct. Mater.* **32**, 2109956 (2022).
- [10] D. A. Harrington and P. van den Driessche, Mechanism and equivalent circuits in electrochemical impedance spectroscopy, *Electrochim. Acta* **56**, 8005 (2011).
- [11] F. Ciucci, Modeling electrochemical impedance spectroscopy, *Curr. Opin. Electrochem.* **13**, 132 (2019).
- [12] D. D. Macdonald, Reflections on the history of electrochemical impedance spectroscopy, *Electrochim. Acta* **51**, 1376 (2006).
- [13] A. Maradesa, B. Py, J. Huang, Y. Lu, P. Iurilli, A. Mrozinski, H. M. Law, Y. Wang, Z. Wang, J. Li, S. Xu, Q. Meyer, J. Liu, C. Brivio, A. Gavriluk, K. Kobayashi, A. Bertei, N. J. Williams, C. Zhao, M. Danzer, M. Zic, P. Wu, V. Yrjänä, S. Pereverzyev, Y. Chen, A. Weber, S. V. Kalinin, J. P. Schmidt, Y. Tsur, B. A. Boukamp, Q. Zhang, M. Gaberšček, R. O'Hayre, and F. Ciucci, Advancing electrochemical impedance analysis through innovations in the distribution of relaxation times method, *Joule* **8**, 1958 (2024).
- [14] Z. Wang, Y. Wang, and F. Ciucci, Distribution of relaxation times: Foundations, methods, diagnostics, and prognosis for electrochemical systems, *Curr. Opin. Electrochem.* **55**, 101789 (2026).
- [15] J. Liu and F. Ciucci, Adaptive distribution of relaxation time analysis using bayesian mixtures, *J. Phys. Chem. C* **129**, 20268 (2025).
- [16] C. Plank, T. Rütther, L. Jahn, M. Schamel, J. P. Schmidt, F. Ciucci, and M. A. Danzer, A review on the distribution of relaxation times analysis: A powerful tool for process identification of electrochemical systems, *J. Power Sources* **594**, 233845 (2024).
- [17] J. Chen, E. Quattrocchi, F. Ciucci, and Y. Chen, Charging processes in lithium-oxygen batteries unraveled through the lens of the distribution of relaxation times, *Chem* **9**, 2267 (2023).
- [18] B. A. Boukamp, Distribution (function) of relaxation times, successor to complex nonlinear least squares analysis of electrochemical impedance spectroscopy?, *J. Phys.: Energy* **2**, 042001 (2020).
- [19] R. Garrappa, F. Mainardi, and M. Guido, Models of dielectric relaxation based on completely monotone functions, *Fract. Calc. Appl. Anal.* **19**, 1105 (2016).
- [20] M. A. Danzer, Generalized distribution of relaxation times analysis for the characterization of impedance spectra, *Batteries* **5** (2019).
- [21] J. Weese, A reliable and fast method for the solution of fredholm integral equations of the first kind based on tikhonov regularization, *Comput. Phys. Commun.* **69**, 99 (1992).
- [22] B. A. Boukamp and A. Rolle, Analysis and application of distribution of relaxation times in solid state ionics, *Solid State Ionics* **302**, 12 (2017).
- [23] B. Py, Z. Wang, Y. Wang, and F. Ciucci, Entropy-based regularized regression for advanced distribution of relaxation times deconvolution, *J. Power Sources* **644**, 236910 (2025).
- [24] B. A. Boukamp, Fourier transform distribution function of relaxation times; application and limitations, Elec-

- trochim. Acta **154**, 35 (2015).
- [25] B. Py, A. Maradesa, and F. Ciucci, From theory to practice: Unlocking the distribution of capacitive times in electrochemical impedance spectroscopy, *Electrochim. Acta* **479**, 143741 (2024).
- [26] J. Song and M. Z. Bazant, Electrochemical impedance imaging via the distribution of diffusion times, *Phys. Rev. Lett.* **120**, 116001 (2018).
- [27] A. Allagui and A. Elwakil, Generalized distribution function of relaxation times with the Davidson-Cole model as a kernel, *Adv. Theor. Simul.* **8**, e00792 (2025).
- [28] N. Florsch, A. Revil, and C. Camerlynck, Inversion of generalized relaxation time distributions with optimized damping parameter, *J. Appl. Geophys.* **109**, 119 (2014).
- [29] J. D. Huang, C. Meisel, N. P. Sullivan, A. Zakutayev, and R. O'Hayre, Rapid mapping of electrochemical processes in energy-conversion devices, *Joule* **8**, 2049 (2024).
- [30] H. Bateman *et al.*, *Tables of integral transforms* (McGraw-Hill Book Company, 1954).
- [31] K. Fung, Generalized mellin transforms i, *Scientia Sinica* **7**, 582 (1958).
- [32] J. Bertrand, P. Bertrand, and J.-P. Ovarlez, *The mellin transform* (CRC Press, 2000) Chap. 11, 2nd ed.
- [33] T. Irino and R. D. Patterson, Segregating information about the size and shape of the vocal tract using a time-domain auditory model: The stabilised wavelet-mellin transform, *Speech Commun.* **36**, 181 (2002).
- [34] L. Knockaert, Fast hankel transform by fast sine and cosine transforms: the mellin connection, *IEEE Trans. Signal Process.* **48**, 1695 (2000).
- [35] A. De Sena and D. Rocchesso, A fast mellin and scale transform, *EURASIP J. Adv. Signal Process.* **2007**, 089170 (2007).
- [36] A. Allagui and A. S. Elwakil, Procedure for obtaining the analytical distribution function of relaxation times for the analysis of impedance spectra using the fox h -function, *J. Phys. Chem. C* **128**, 2788 (2024).
- [37] D. W. Davidson and R. H. Cole, Dielectric relaxation in glycerol, propylene glycol, and n-propanol, *J. Chem. Phys.* **19**, 1484 (1951).
- [38] The Mathematical Functions Site, Hyperbolic tangent, series representation (2025).
- [39] M. Saccoccio, T. H. Wan, C. Chen, and F. Ciucci, Optimal regularization in distribution of relaxation times applied to electrochemical impedance spectroscopy: Ridge and lasso regression methods - a theoretical and experimental study, *Electrochim. Acta* **147**, 470 (2014).